Article

Biological activity and nanostructuration of Fe_3O_4-Ag /polypropylene nanocomposites

Phuong Nguyen-Tri

[1] Department of Chemistry, University of Montréal, Quebec, Canada;
Email: Phuong.nguyen.tri@umontreal.ca (P. Nguyen-Tri); Tel. + 514-340 5121 (7326):

Abstract: We report here the synthesis of uniform nanospheres-like silver nanoparticles (AgNPs, 5-10 nm) and the dumbbell-like Fe_3O_4-Ag hybrid nanoparticles (FeAgNPs, 8-16 nm) by the use of seeding growth method in the presence of oleic acid (OA)/ oleylamine (OLA) as surfactants. The antibacterial activity of pure nanoparticles and nanocomposites by monitoring the bacterial lag–log growth has been investigated. The electron transfer from AgNPs to Fe_3O_4NPs which enhances the biological of silver nanoparticles has been proven by nanoscale Raman spectroscopy. The lamellae structure in the spherulite of FeAgNPs/PE nanocomposites seems play the key role to the antibacterial activity of nanocomposites, which has been proven by nanoscale AFM-IR. An atomic force microscopy coupled with nanoscale infrared microscopy (AFM-IR) is use to highlight the distribution of nanoparticles on the surface of nanocomposite at the nanoscale. The presence of FeAgNPs in PE nanocomposites has a better antibacterial activity than that reinforced by AgNPs due to the faster Ag+ release rate from the Fe_3O_4-Ag hybrid nanoparticles and the ionization of AgNPs in hybrid nanostructure.

Keywords: Polyethylene, nanocomposites, silver nanoparticles, Fe_3O_4-Ag hybrid nanoparticles, antibacterial activity

1. Introduction

The transmission of infectious diseases by bacteria in in airports, hospitals and other public places is increasing in the last few decades[1]. The development of self-sterilizing polymers[2-3] able to inactivate bacteria loaded with antibacterial agents is a way to increase the bactericide performance of surfaces designed to disinfect spaces spreading the infections due to toxic biofilms. *E. coli* has been reported to lead food poisoning[4-5]. Silver nanoparticles are reported to be effective biocidal agents against various bacteria[6-9]. The recent report approved that the antibacterial activity comes from silver ions (Ag+), not from Ag metallic[6]. Different components are combined with silver to yield a nanoentity with desired properties not afforded by their counterparts. For example, combination of Ferrite and silver is expected to enhance the antibacterial activity due to the electron transfer between two these metals and thus enhances the release of silver ions, the main against for the inactivation of bacteria and virus. The magnetic properties of ferrite leads to the formation of superparamagnetic composites which are useful in carcinoembryonic antigen in clinical immunoassay[10] and water treatment due to its enable easy separation from solution[11].

The biological activity of silver can be enhanced in combination with other transition metals such as nano-silver-ferrite composite[12] The highest antibacterial effect of 99.4% was achieved at 5.4 wt % of NPs and the driving frequency of 100 rpm. A time-dependent antibacterial effect in 0.1 wt % of Ag/Fe3O4 was also observed which indicated that the use of specific rotating magnetic fields to manipulate Ag/Fe_3O_4 magnetic NPs can significantly improve the antibacterial efficacy to *E Coli* and the highest antibacterial effect can be achived to 99.4%. The antibacterial silk from Fe3O4-Ag have with have high antibacterial activities against both Escherichia coli and Staphylococcus aureus been also synthesized[13]. The author confirmed that the as prepared antibacterial silks be easily recycled

without a decrease in their antibacterial activities due to the synergistic effects between the Ag NPs and Fe_3O_4 NPs with large amounts of active sites[13]. Depending on synthesis conditions, various morphologies of hybrid nanoparticles can be achieved[14-16].

Polypropylene is one of the most common polyolefin and remains the most consumed polymer in the world due to its interesting good mechanical properties, its stability and its low cost[14, 17-22]. The addition of additive brings this polymer various new properties depending on end-end applications[23-25]. Here, the main goal of this word is to prepare of the hybrid silver nanoparticles with high antibacterial activity and then incorporated in the polyethylene matrix and investigate its antibacterial activity. Some recent pointed techniques such as atomic force microscopy coupled with nanoscale infrared (AFM-IR) and nanoscale Raman (AFM-Raman) will be used for better understanding the release behavior on the composite surfaces and propose the possible mechanism for the enhancement of the antibacterial activity.

The atomic force microscope (AFM) has been widely used for the study of nanocomposites and polymeric materials with nanoscale spatial resolution[26-33]. AFM-IR allows surface mapping with a resolution of several tens of nanometers. The main limitation of AFM-IR concerns the laser source near infrared (900-4000 cm^{-1}) region. Detection of the bonding signals between polymer and metals appearing below 900 cm^{-1} cannot be detected. The nano-Raman can overcome these drawbacks. AFM-Raman combines confocal Raman spectroscopy and imaging providing specific chemical information on the nano-materials with a sub-micron spatial resolution[34-37].

We show in this study that AFM-IR and AFM-Raman can be used to investigate the nanoscale structure and the electron transfer in hybrid nanoparticles. The detailed microstructure of FeAgNP and PE nanocomposites containing Fe_3O_4-Ag hybrid nanoparticles is addressed in this study. The release mechanism was investigated when these nanoparticles were incorporated in PE. The effect of these nanoparticles on the lamellae structure of PE was also worked out in the course of this study.

2. Materials and Methods

2.1. Chemicals

Iron(III) acetylacetonate (Fe(acac)3) 99.99 %; silver nitrate (AgNO3) 99 %; sodium borohydride (NaBH4) 99 % and sodium stearate 99 %; solvents: 1-octadecene, di-chlorobenezene (DCB, 99 %), absolute ethanol and hexane; surfactants and reductant: oleic acid (OA) 99 %, oleylamine (OLA) 70 %, 1,2 n-hexadecanediol (HDD) 90 %, polyvinylpyrrolidone (PVP) were purchased from Sigma-Aldrich. HDPE granules were purchased from IRPC Public Company (grade G2855 – Polimaxx Polene, Thailand).

2.2. Synthesis of nanoparticles

AgNPs were prepared by the reduction of silver nitrate using sodium borohydride in the presence of PVP in distilled water. A 20 mL volume of 5 mM silver nitrate was added dropwise to 200 mM of PVP (at 0.1 wt.%), then 50 mL of 10 mM chilled sodium borohydride solution was added drop-wise into the above mixture. The reaction mixture was stirred vigorously during 30 min by using a magnetic stirring plate and sonicated for another 30 min. Afterwards, the AgNPs was extracted with 100 mL xylene at 50 °C.

Synthesis of Fe3O4 nanoparticles: the Fe3O4 nanoparticles (Fe3O4 NPs) were prepared by pouring cetylacetonate (0.162 g, 0.63 mM), Fe (III) acetylacetonate (0.6 g, 1.9 mM) and hexadecanediol (0.58 g, 1.5 mM) into a 100 mL three-neck flask. At the same time, 3.6 mL OA, 3.6 mL OLA and 30 mL 1-octadecene were added into the above mixture. The concentrations of Fe(acac)3, OA, OLA, and HDD in the solution were equal to 63, 372, 372 and 75 mM, respectively. The reaction mixture was stirred and degassed at room temperature for 30 min before heating to 100 C, and kept at this temperature for 30 min to remove water. The temperature was increased to 200 C, and kept for 30 min. Then, the reaction solution was heated further to 295 C at a heating rate of 5-7 C/min and maintained for 30 min before cooling to room temperature. The Fe3O4 NPs were then purified from the excess ligands before the synthesis of Fe3O4-Ag as follows: 20 mL of the Fe3O4 NPs

solution was mixed with 20 mL of ethanol. The Fe3O4 NPs were then collected using a magnetic bar and the supernatant was discarded. The Fe3O4 NPs were thereafter dispersed in 5 mL hexane and precipitated by adding 5 mL of ethanol. The precipitation/re-dispersion procedure was repeated two more times and the Fe_3O_4 NPs were finally dispersed in DCB.

Synthesis of Fe_3O_4-Ag hybrid nanoparticles: The seeding growth method was used to prepare Fe3O4-Ag NPs. About 5 mL of DCB solution containing 500 mg AgNO3 and 3 mL OLA was added drop-wise into 20 mL DCB containing 100 mg purified Fe3O4 NPs (at 170 °C). The mixture was maintained at this temperature for 60 min before cooling to room temperature.

2.3. Preparation of nanocomposites

The master batch of PE nanocomposites containing a high concentration of nanoparticles (2 wt. %) was prepared by the mixing method. PE granules were dissolved in toluene (5 wt. %, stirring at 85 °C). The nanoparticles were then added to this solution following a sonication during 1h. Toluene was then removed at (110 °C) under vacuum. To fabricate the final PE nanocomposite sheets, the above as-prepared master batch was mixed with PE granules, and then blended in an internal HAAKE mixer at 50 rpm and 170 °C for 8 min to extrude the final PE nanocomposites containing 0.1 wt. % of AgNPs.

To characterize the polymer nanostructure, a solution of 20 mg/ml was added in 1,2 dichlorobenzene and stirring during 24h, then heated up to 90 °C in the dark before casting it over Si-wafer or gold substrates. Polymer films were dried under vacuum at 60 °C for 2 h to ensure complete removal of residual solvent. The polymer film was then melted at 180 °C during 3 min to ensure transformation to crystalline crystals and subsequently quenched to the selected crystallization temperature at a cooling rate of 100 °C/min.

2.4. AFM-IR

The AFM-IR measurements were carried on a Nano-IR2 system (Anasys Instruments, CA, USA). The AFM images were recorded in contact mode at a rate line 0.1-1 Hz using a gold-plated silicon nitride probe (Anasys Instruments, CA, USA) with an elastic constant of about 0.5 $N.m^{-1}$ and nominal radius of 10 nm. The nanoscale IR spectra were collected directly on the single fiber surface, deposited on double-side adhesive tape within the 900-3600 cm-1 range at a spectral resolution of 4 cm-1, 256 co-averages. The single IR radiation image is recorded with a scan rate of 0.1 Hz, resolution 1024 x 1024 pixels and 16 co-averages, at a power limit within 0.5-4 % at a frequency of 196 Hz. All measurements were carried out at room temperature in a room provided with humidity controller (about 20 % RH). This precludes the effect of water absorption on the sample surface during the analyzing. The nano-IR devices were located in an anti-vibration system.

2.5. AFM-Raman

The Raman spectra and AFM images were recorded on a Witec Alpha300 RSA unit equipped with an AFM & SNOM Confocal Raman Microscope. The AFM images were recorded in contact mode with a rate of 0.3 Hz using an AFM tip TESPA (Brucker, CA, USA). For nano-Raman spectra measurements, the integration time was about 1s with 10 scans at a spectral resolution of 1 cm-1 and laser wavelength of 532 nm. The laser power was set at 15 mW to avoid sample burning.

2.6. UV-Vis analysis

An UV–Vis spectrophotometer, model CINTRA 4040 (GBC, USA) with 2 nm slit width was used to monitor the absorbance of the chromophores and the electron transfer in the nanocomposites.

2.7. Antibacterial growth test

E. coli DH5α bacteria were purchased from Invitrogen (USA). Luria- Broth medium was provided by Merck (Germany). To evaluate the cell density, a Beckman Coulter DU-730 (USA) was

used. In this test, the optical density OD600 measures the light absorbance of the E. coli sample. Different cell strains may have different cell numbers at a given OD600 value, but OD600 = 1 usually means that there are about 1x109 cells per ml culture. Bacterial pre-cultures were prepared to generate subcultures of bacterial in the lag phase so that the number of bacterial cells was constant before the log phase or exponential growth phase. In this way, the growth rate of the bacteria on the nanocomposites was evaluated. The OD600 values in the range 0.1–2.0 for cell densities of E. coli culture indicated the bacterial growth rates.

A volume of 100 μL of stock culture of E. coli in glycerol was pipetted into 3 mL of medium in a 15 mL test tube and shaken overnight at 200 rpm and 37 °C. Afterward, a 500 μL aliquot of pre-culture was inoculated into 100 mL of medium in a 500 mL Erlenmeyer flask and shaken at 200 rpm and 37 °C until the OD600 absorbance value reached 0.3. These pre-cultures were used to account for the bacterial growth rate.

The as-prepared nanocomposites were cut into 10×10 mm square samples and then washed with acetone to remove all impurities on the sample surface and autoclaved at 130 ˚C for 20 min before every test.

The monitoring test for the evaluation of the bacterial growth was adapted from procedures described in the ASTM E 2149-10 standard. Ten square samples of autoclaved nanocomposites were placed into each 100 mL bacterial pre-culture in a 500 mL Erlenmeyer flask (as described previously) in which the OD600 had reached 0.3 and shaking was continued at 200 rpm at 37 °C. Then, the OD600 values of the bacterial cultures were monitored every 30 min until OD reached 2.0. The reported data was the average of three cultures. The relative OD600 values were then standardized to evaluate the effect of the nanocomposites on the growth rate of the bacteria. The pure bacterial cultures were used as controls.

3. Results and discussion

3.1. Characterization of nanoparticles

Figure 1 shows the TEM images of Fe_3O_4NPs (Fig. 1a), FeAgNPs (Fig. 1b and 1c) dispersed in an organic solvent (DCB). Figure 1a shows the uniform particle distribution with a diameter of 6-8 nm. Figure 1c shows that hybrid FeAgNPs with a uniform dumbbell-like structure: the bigger nanoparticles are AgNPs and the smaller ones are Fe3O4NPs. It has to be noted that, the synthesis process of hybrid nanoparticles was optimized to attain the reported sizes of the hybrid nanoparticles.

The Fe_3O_4NPs were synthesized and used as the seeding components before hybridization with AgNPs; the average size of Fe_3O_4NPs (about 6-8 nm) was not affected during the hybridization process with AgNPs. Bigger sizes of AgNPs with an average about 15-16 nm were expected. During the breeding processes both the temperature (170 ˚C) and an Ag-salt concentration 10 times higher than the volume of Fe_3O_4 nanoparticles. The synthesis of dumbell Ag- Fe_3O_4 hybrid systems with an AgNPs size of about of 15-16 nm may be used as template to fabricate Au (hollow)-Fe_3O_4 in which a plasmon-resonance peak in the near infrared region could be of interest for novel optical imaging applications.

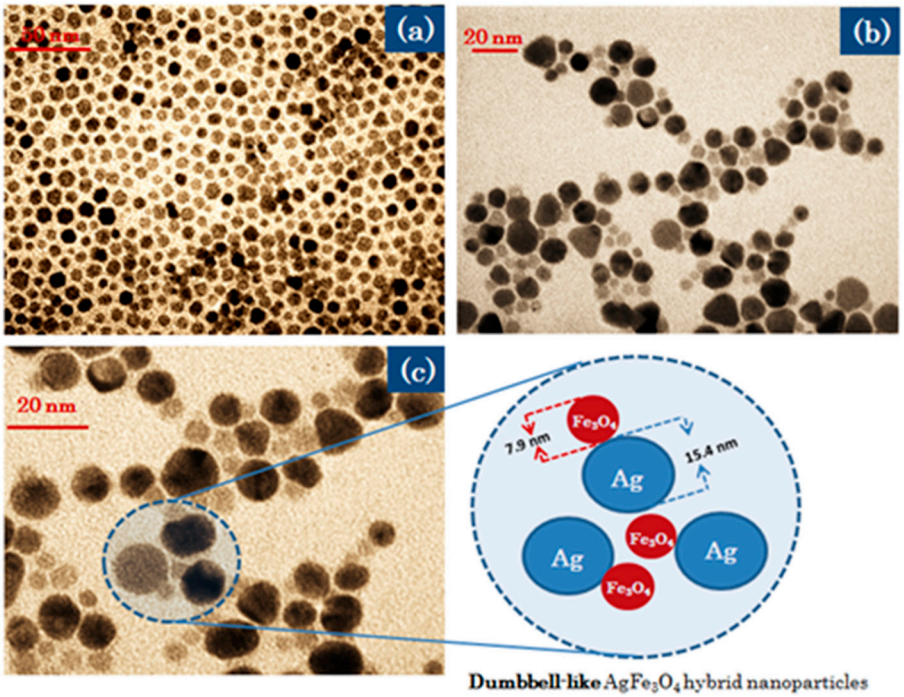

Figure 1. TEM images of OL/OLA coated Fe3O4NPs (a) and FeAgNPs (b, c) dispersed in DBC.

UV-Vis spectra of OL/OLA coated Fe3O4 NPs, AgNPs and FeAgNPs were carried out and the results are shown in Figure 2. A broad absorption band in the region of 300–600 nm for Fe_3O_4NPs was observed,[38] the shoulder at ~360.8 nm was due to nanosized Fe_3O_4NPs.[39] The band around 400 nm is characteristic for the surface Plasmon resonance (SPR) peak of AgNPs[40].

The hybridization of AgNPs and Fe_3O_4NPs leads to a red shift in the SPR spectra and a significant broadening of the SPR peak. AgNPs, SPR peak is located at 398.5 nm, and at 415.5 nm for the Fe_3O_4-Ag hybrids. This red shift is assigned to the electron transfer between both samples leading to a depletion of the free electron density in the surface layer due to the increase of π back bonding with the ligand.[41-42] In contrast, the presence of electron donors induces a blue-shift of SPR.[43-44]The contribution of Fe3O4NPs nanoparticles gives raise to a band at ~360 nm. The peak at 617.8 nm could be assigned to the hybridization of AgNPs and Fe_3O_4 NPs.

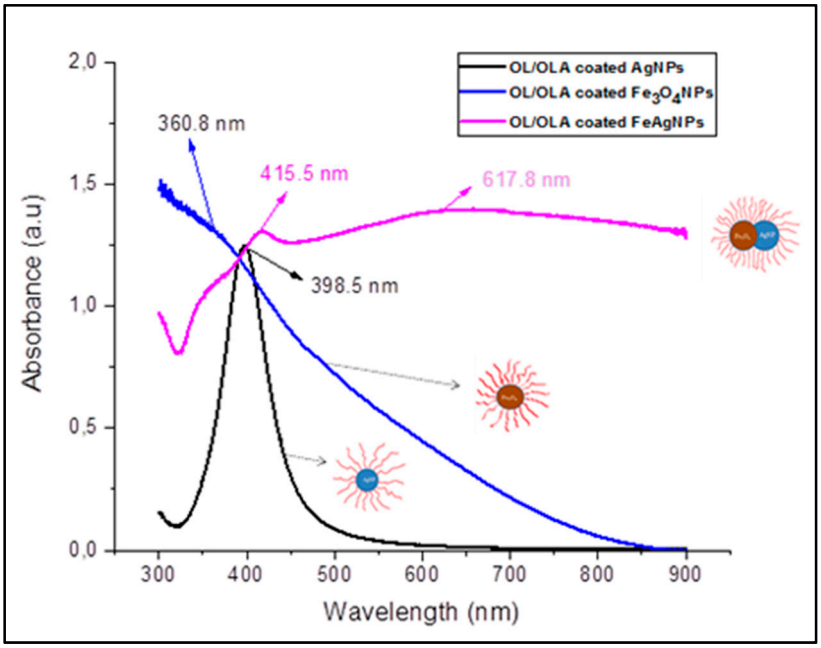

194 ***Figure 2.*** UV-visible absorption spectra of the OL/OLA coated Fe3O4 NPs, PVP coated AgNPs and
195 OL/OLA coated FeAgNPs hybrid nanoparticles dispersed in hexane.

196 *3.2. Antibacterial behavior of HDPE nanocomposites*

197 Figure 3 shows the effect of the PE/AgNPs and PE/FAgNPs nanocomposites on the growth rate
198 of E. coli liquid cultures. It shows that the growth rates of the pure cultures and mixed cultures with
199 PE slow down after 4h of cultivation. The log phases of the pure cultures and mixed cultures with
200 neat PE are about 93% after 1h cultivation, whereas they are 85 % in the case of mixed cultures with
201 PE/AgNPs. Thus, the E. coli bacterial growth is inhibited by the presence of PE/AgNPs
202 nanocomposites. PE/FeAgNP growth rates of the culture were 81 % after 4h. The presence of
203 FeAgNPs in the PE matrix exhibits a higher antibacterial activity, as compared to the AgNPs. The
204 FeAgNPs had showed a higher bactericidal activity against staphylococcus aureus bacteria
205 compared to AgNPs 28 due to: i) a high catalytic activity of AgNPs dispersion and stability due to
206 the Fe3O4 carrier, and ii) a large surface contact area between the bacterial cell membrane and the
207 hybrid nanoparticles.

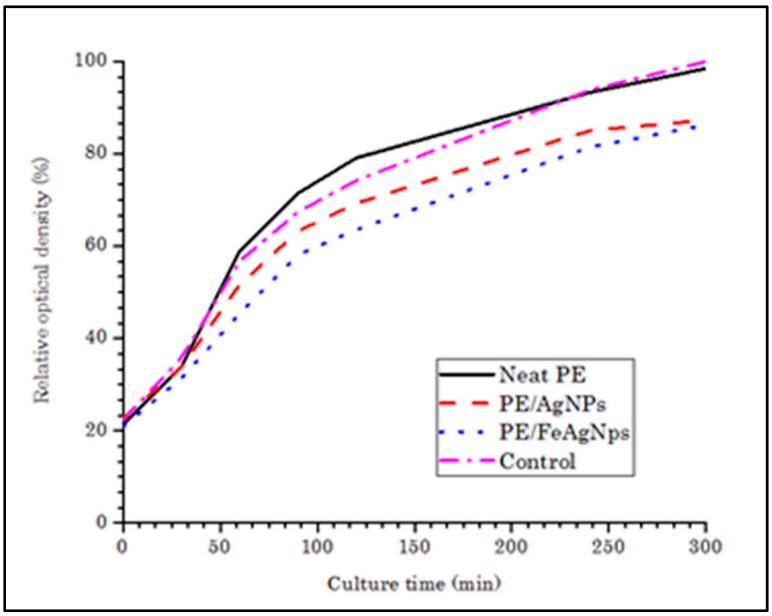

208

209 ***Figure 3.*** Growth rate of E. coli liquid cultures of neat PE and nanocomposites with AgNPs and
210 hybrid FeAgNPs. The data shown represent the average of three cultures (standard deviation < 2 %).

211 Since the average size of AgNPs in FeAgNPs was bigger than that of AgNPs, the above findings
212 may be due to the faster Ag^{+} release rate from the Fe_3O_4-Ag hybrid nanoparticles. It was suggested
213 that the ionization of AgNPs in hybrid nanostructure was be accelerated by Fe^{3+} ions. It has reported
214 that addition of Ag and Fe^{3+} enhances the bio-leaching efficiency of the As-bearing gold ore and the
215 electron transfer from Ag-core to the FeCo shell in 15 nm hybrid nanoparticles which are proven by
216 XPS results[45].

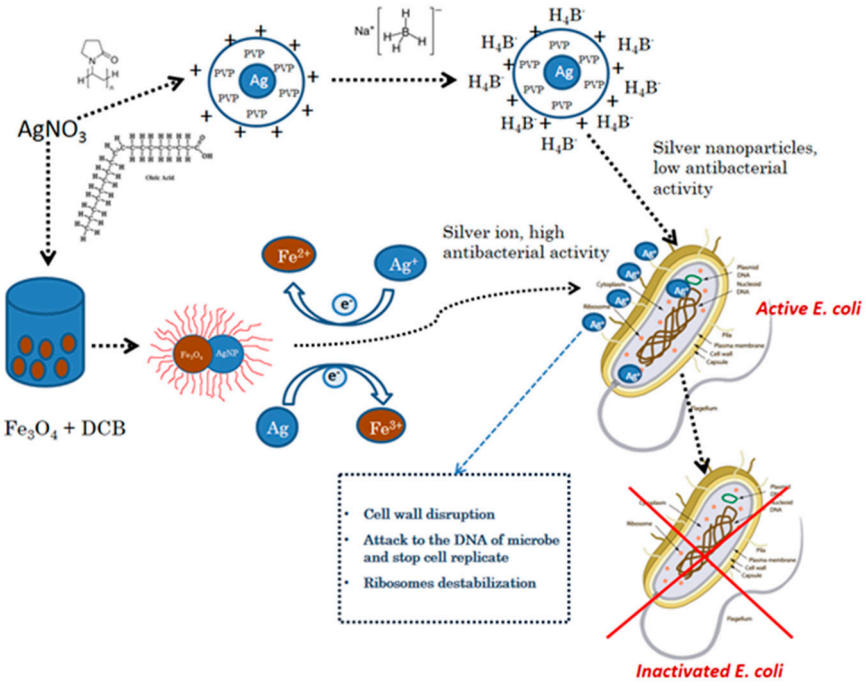

Figure 4. Mechanism of inactivation of E. coli by FeAgNPs in which the electron exchange between AgNPs and FeNPs promotes the formation of the Ag+-ion leading to inactivation of E. coli.

It is widely accepted that nano-silver interacts with bacterial membranes and causes cell wall disruption.[46-47] The AgNPs absorbed on the outer bacteria membrane surface penetrates into the cytoplasm and inhibits cell replication[48]. The AgNPs simultaneously induce apoptosis and inhibit DNA synthesis due to the silver ions (Ag^+)[49]. Oxidation/reduction of silver ions and Fe^+ promoting the release of silver ions to kill bacteria would proceed. In a reversible process, the concentration of silver ions remained stable in hybrid nanoparticles showing a higher antibacterial activity compared to AgNPs. Based on the results mentioned above, we suggest a novel mechanism of the inactivation of bacteria by FeAgNPs hybrids. The Ag^+ would intervene in a reversible electron transfer to Fe^{3+} (Fig. 4).

3.3. Nanoscale architecture of PE /FeAgNPs nanocomposites

Figure 5 shows the morphology of the PE/FeAgNPs of neat PE and PE/FeAgNPs nanocomposites. The nanocomposites present a very different structure compared to that of neat PE in which the PE exhibits banded spherulites with sizes from 10-20 μm. The formation of ring-banded spherulites of semi-crystalline polymers is well known. The concerted twisting of the crystallographic orientation takes place during lamella growth under effect of surface stress but the arrangement of lamella in the banded spherulites is still an open question. It has been suggested that lamella stacks were continuously twisted up and down to create of ridge and valley banded spherulites, respectively. The valley areas are basically composed by plat-on lamella while the edge-on lamellas are present in ridge areas. However, this band structure is not observed in the case of PE/FeAgNPs nanocomposites. This can be attributed to nanoparticles acting as a nucleation agent for the crystallization at an early stage of the crystallization. This can explain why the nanocomposites possess a higher spherulite density with smaller sizes compared to those of neat PE. It is interesting that the PE/FeAgNPs structure of spherulites was mainly composed by edge on lamella with a growth direction perpendicular to the substrate. This structure gives a more suitable configuration for the release of nanoparticles during the antibacterial tests. The IR spectra in Figure 5 (left and right sides) show that the main vibrational peaks appearing in the IR spectra of neat PE are similar to those measured by the traditional FT-IR microscope related to the intensity and position. The bands at 2924 and 2874 cm^{-1} are assigned to the vibration of symmetric and asymmetric methylene groups. These bands shift to lower frequencies in the case of nanocomposites due to the

contribution of long alkyl chain of oleic acid and oleylamine of the nanoparticles coating. The vibrational bands at 1461, 1396 and 1368 cm^{-1}, assigned to CH_2 bending, CH_3 bending and CH_2 wagging, respectively, shift to lower frequencies in the nanocomposites. Particularly, a new peak at about 1245 cm^{-1} is observed in the case of nanocomposites which is slightly different to that observed in the case of pure nanoparticles at about 1225 cm^{-1}. This band is probably due to the presence of C-O stretching in the ester and H bonded hydroxyl group stretching.[50] The appearance of the peak at 1245 cm^{-1} is important to identify the presence of nanoparticles near the sample surface of the nanocomposites and it can be used as a marker to detect nanocomposites in PE matrix.

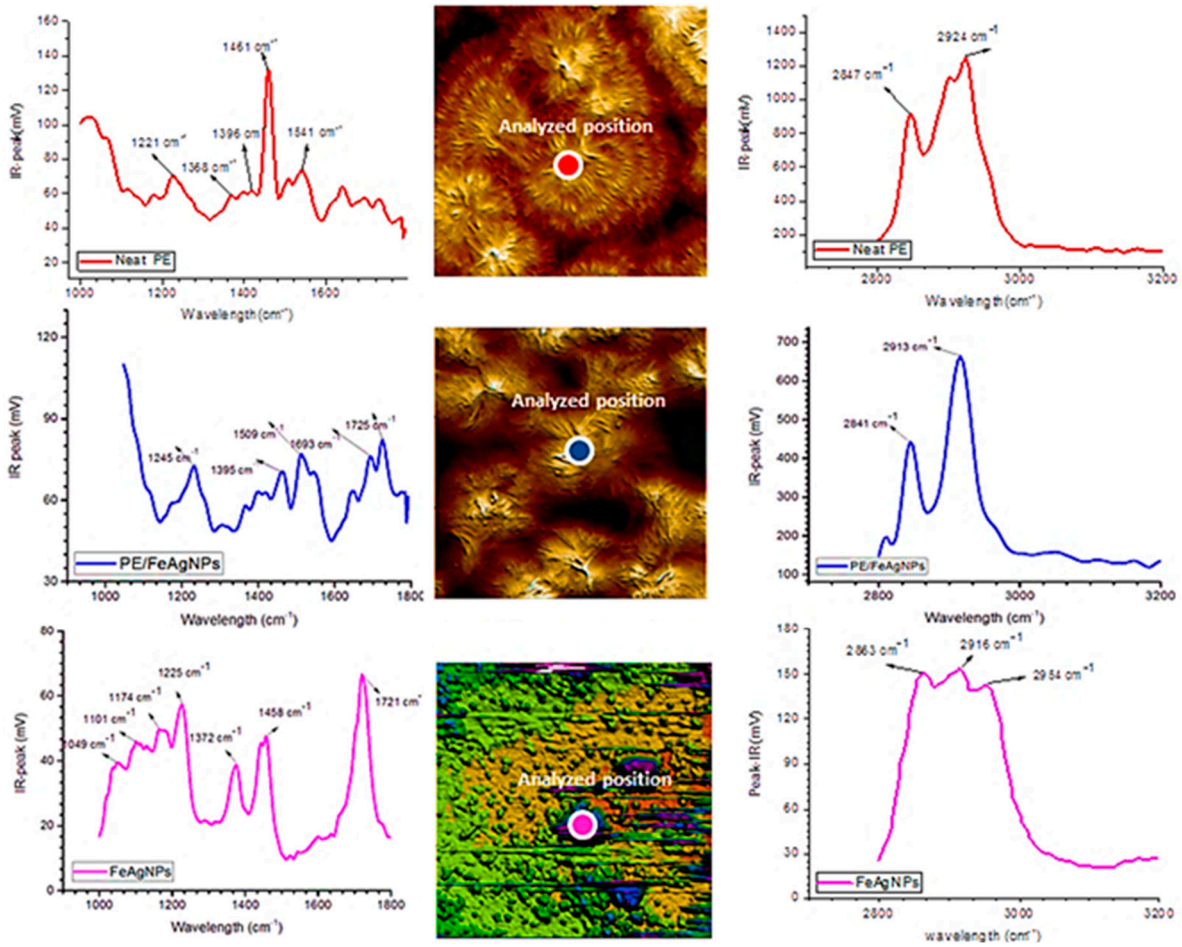

Figure 5. Nano-IR spectra of neat PE, PE/FeAgNPs nanocomposites and pure dumbbell like-FeAgNPs. The middle column shows AFM images at the position at which the IR spectra were analyzed. Sample thicknesses were about 500 nm and films were deposed on gold substrates.

Figure 6 shows high-resolution AFM images of neat PE and the surface nanocomposites. The morphology of the spherulites is shown in Figure 5, but not the contour of the nanoparticle surface. The presence of nanoparticles on the sample was therefore determined by IR-spectroscopy. The peak at 1245 cm^{-1} was assigned to the C-O stretching in the OL/OLA layer (P1-P3), but it is absent in neat PE as shown in Figure 7. The distribution of nanoparticles was obtained by TEM.

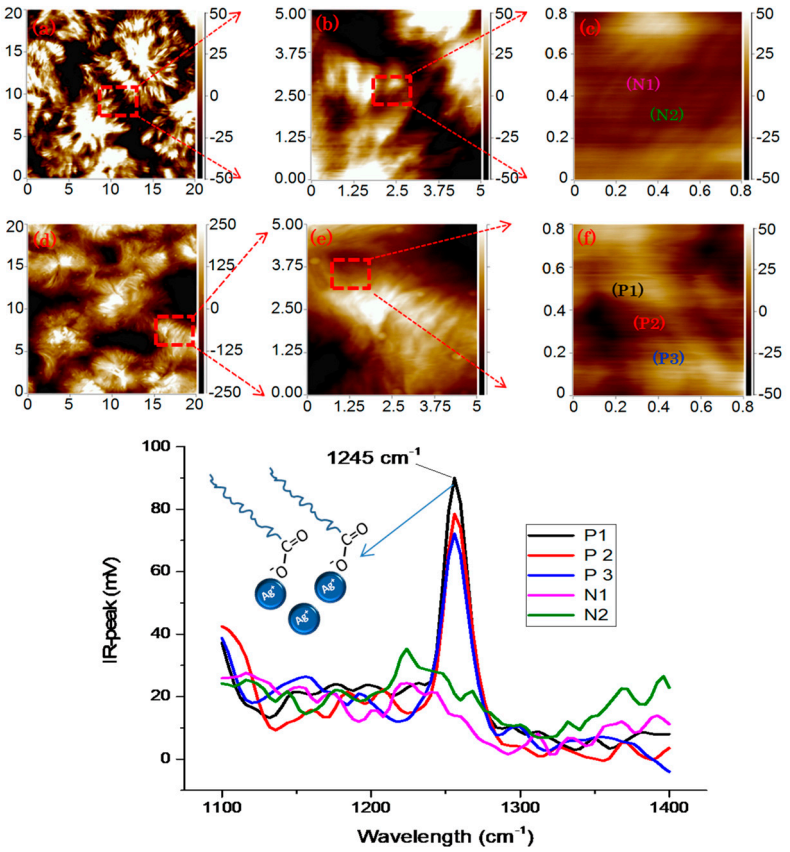

Figure 6. High-resolution AFM images of neat PE at different magnifications (a, b, c); high-resolution AFM images of morphology of PE/FeAgNPs nanocomposites (d, e, f) and IR spectra (Figure 6g) of neat PE at position N1 and N2, the spectra of PE/FeAgNPs nanocomposites at different positions P1, P2, P3.

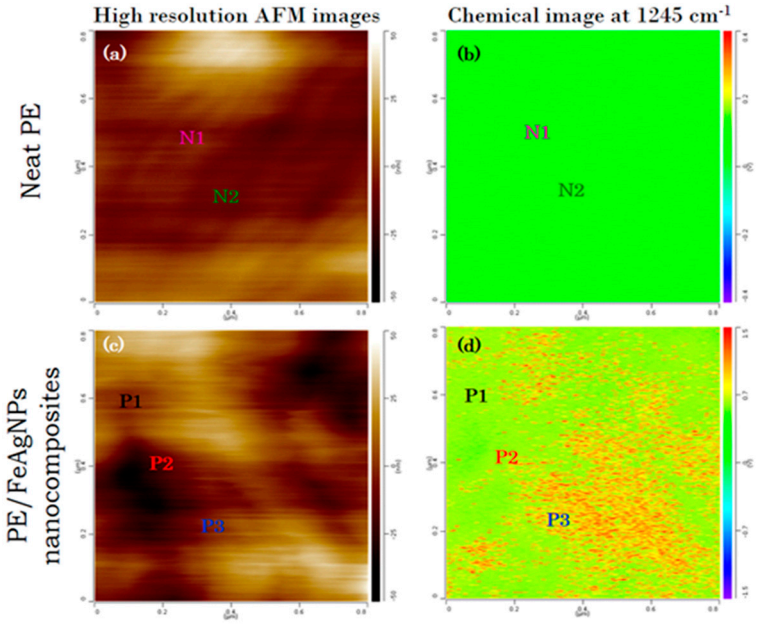

Figure 7. a) high resolution AFM images of neat PE; b) IR-mapping image of neat PE; c) high resolution AFM images of PE/FeAgNPs nanocomposites; d) IR mapping image of PE/FeAgNPs nanocomposites. The points N1, N2, P1, P2, P3 are points corresponding to the nano-spectra analysis described below in Figure 8 c, f. Film thickness was close to 500 nm, deposed on Si-wafer substrate.

Resonance enhanced IR-spectroscopy single beam mode was used to obtain a dimensional mapping image of C-O stretching at 1245 cm^{-1} in the area shown in Figure 7. In the case of neat PE, IR- absorption mapping at 1245 cm^{-1} was observed to be negligible. The band was absent in neat PE shown in Figures 6c and 6g. However, for the PE/FeAgNPs nanocomposites, the absorption of C-O stretching was observed. In fact, there are some domains in which, the IR-absorption of C-O was strong. This high vibrational absorption was due to the presence of OL/OLA on the surface of hybrid nanoparticles. For the first time nanoparticles are detected on a polymer matrix in the nanoscale without using of TEM technique. This is a non-destructive method for the characterization of nanoparticles dispersed on a polymer matrix.

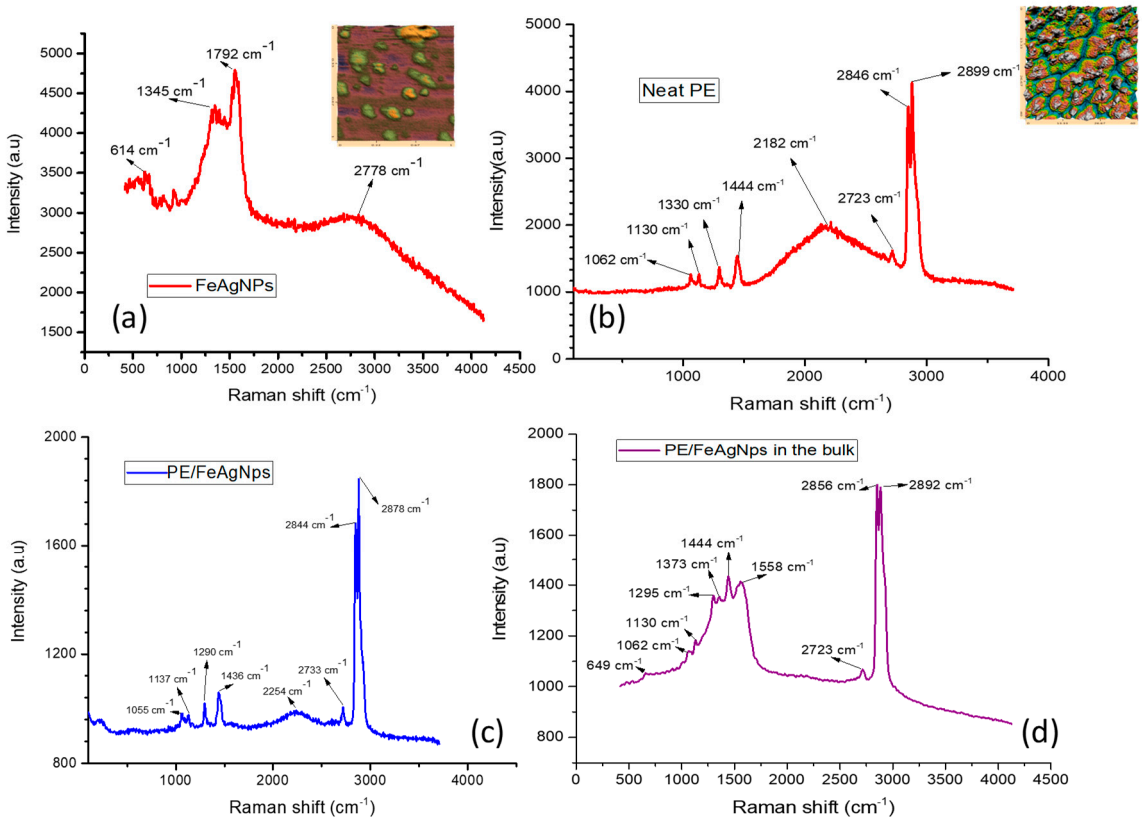

Figure 8. Raman spectra of neat PE, FeAgNPs and PE/FeAgNPs, nanocomposites with high-resolution AFM images. Right hand images show the position of FeAgNPs together with the spectra of neat PE, PE/FeAgNPs and PE/FeAgNPs nanocomposites. Nano-Raman spectra are shown on the left-hand side.

Figure 8 shows the AFM-Raman spectra and AFM images with the characteristic bands for FeAgNPs located at 1792, 1345 and 614 cm^{-1}. It is interesting to see that the typical Raman shift of magnetite Fe3O4 around 668-670cm^{-1} was not observed in both FeAgNPs and nanocomposites.[51] However, two new bands at 613 and 1345 cm^{-1} appeared and were assigned to the Raman vibrational peaks of α-Fe_2O_3.[52] These bands were visible on FeAgNPs alone and in the nanocomposite films. This may involve the phase transformation from Fe_3O_4 to α-Fe_2O_3 hexagonal plates. In other words, the electron transfer from AgNPs to Fe_3O_4 leads to the reduction from Fe^{3+} to Fe^{2+} ions during the nucleation/growth of Fe_3O_4 polyhedral particles as described above in Figure 4. The broadening of the peak at 1792 and 2778 cm^{-1} is due to the vibrational of carbonyl group and methylene group in the structure of oleic acid[53]. In neat PE, characteristic Raman vibrational bands are seen at 1060 and 1130 cm^{-1} and both are assigned to C-C stretching; the bands at 1295, 1444, 2846, 2899 cm^{-1} are assigned to methylene twisting, CH_2 wagging and asymmetric and symmetric CH_2 stretching vibrations. The shift to lower frequencies is due to the change in the crystallinity and of the lamella

assembly on the PE-surface. Two new bands observed at 1558 and 1373 cm^{-1} in the Raman spectrogram of the PE/FeAgNPs particles, but could not be assigned at the present time.

4. Conclusions

This study presents the synthesis of new and uniform hybrid nanoparticles nano-spheres of AgNPs (6-8 nm) and dumbbell like-hybrid FeAgNPs (15-16 nm). The activity was evaluated when they are incorporated a polyolefin. By resonance enhanced atomic force microscopy coupled infrared spectroscopy (nano-IR), it was possible to detect and identify the distribution of the nanoparticles in the polymer matrix. The lamella assembly and the spherulite structure of PE/FeAgNPs are also examined. AFM-Raman spectra of the nanocomposites provide useful information about electron-transfer mechanism of the hybrid nanoparticles, resulting in a higher antibacterial activity. The electron-transfer would proceed from hybrid FeAgNPs and AgNPs to Fe_3O_4NPs in a reversible fashion. The ionization of AgNPs in hybrid nanostructure might be accelerated by Fe^{3+} ions. The as- prepared nanocomposites exhibit a self-sterilizing property, avoiding the formation of biofilms the most dangerous source able to spread for long times toxic bacteria into the environment.

Author Contributions: P.N.T and S. R. contributed equally to this work

Funding: This work was financial supported by Natural Sciences and Engineering Research Council of Canada (NSERC) and the Vietnam Academy of Science and Technology (VAST). This work was also partly supported by NAFOSTED (grant 103.02-2012.74).

Acknowledgments: We thank Patricia (University of Montreal, Canada) for help with the AFM-IR measurements.

Conflicts of Interest: The authors declare no conflict of interest

References

1. Wang, L.-S.; Gupta, A.; Rotello, V. M., Nanomaterials for the Treatment of Bacterial Biofilms. *ACS Infectious Diseases* **2016,** *2* (1), 3-4.
2. Pappas, H. C.; Phan, S.; Yoon, S.; Edens, L. E.; Meng, X.; Schanze, K. S.; Whitten, D. G.; Keller, D. J., Self-Sterilizing, Self-Cleaning Mixed Polymeric Multifunctional Antimicrobial Surfaces. *ACS Applied Materials & Interfaces* **2015,** *7* (50), 27632-27638.
3. Hui, L.; Su, Y.; Ye, T.; Liu, Z.; Tian, Q.; He, C.; Zhao, Y.; Chen, P.; Wang, X.; Han, W.; Luo, Y.; Wang, B., Self-Sterilizing and Regeneratable Microchip for the Precise Capture and Recovery of Viable Circulating Tumor Cells from Patients with Cancer. *ACS Applied Materials & Interfaces* **2018,** *10* (1), 207-218.
4. Turner, A.; Chen, S.-N.; Joike, M. K.; Pendland, S. L.; Pauli, G. F.; Farnsworth, N. R., Inhibition of Uropathogenic Escherichia coli by Cranberry Juice: A New Antiadherence Assay. *Journal of Agricultural and Food Chemistry* **2005,** *53* (23), 8940-8947.
5. Osawa, R.; Kamide, T.; Satoh, Y.; Kawano, Y.; Ohtsu, I.; Dairi, T., Heterologous and High Production of Ergothioneine in Escherichia coli. *Journal of Agricultural and Food Chemistry* **2018,** *66* (5), 1191-1196.
6. Xiu, Z.-m.; Zhang, Q.-b.; Puppala, H. L.; Colvin, V. L.; Alvarez, P. J. J., Negligible Particle-Specific Antibacterial Activity of Silver Nanoparticles. *Nano Letters* **2012,** *12* (8), 4271-4275.
7. López-Esparza, J.; Espinosa-Cristóbal, L. F.; Donohue-Cornejo, A.; Reyes-López, S. Y., Antimicrobial Activity of Silver Nanoparticles in Polycaprolactone Nanofibers against Gram-Positive and Gram-Negative Bacteria. *Industrial & Engineering Chemistry Research* **2016,** *55* (49), 12532-12538.
8. Ramalingam, B.; Parandhaman, T.; Das, S. K., Antibacterial Effects of Biosynthesized Silver Nanoparticles on Surface Ultrastructure and Nanomechanical Properties of Gram-Negative Bacteria viz. Escherichia coli and Pseudomonas aeruginosa. *ACS Applied Materials & Interfaces* **2016,** *8* (7), 4963-4976.

9. Taglietti, A.; Diaz Fernandez, Y. A.; Amato, E.; Cucca, L.; Dacarro, G.; Grisoli, P.; Necchi, V.; Pallavicini, P.; Pasotti, L.; Patrini, M., Antibacterial Activity of Glutathione-Coated Silver Nanoparticles against Gram Positive and Gram Negative Bacteria. *Langmuir* **2012,** *28* (21), 8140-8148.
10. Tang, D.; Yuan, R.; Chai, Y., Magnetic Core−Shell Fe3O4@Ag Nanoparticles Coated Carbon Paste Interface for Studies of Carcinoembryonic Antigen in Clinical Immunoassay. *The Journal of Physical Chemistry B* **2006,** *110* (24), 11640-11646.
11. Liu, C. H.; Zhou, Z. D.; Yu, X.; Lv, B. Q.; Mao, J. F.; Xiao, D., Preparation and characterization of Fe3O4/Ag composite magnetic nanoparticles. *Inorganic Materials* **2008,** *44* (3), 291-295.
12. Chang, M.; Lin, W.-S.; Xiao, W.; Chen, Y.-N., Antibacterial Effects of Magnetically-Controlled Ag/Fe3O4 Nanoparticles. *Materials* **2018,** *11* (5).
13. Liu, X.; Yin, G.; Yi, Z.; Duan, T., Silk Fiber as the Support and Reductant for the Facile Synthesis of Ag–Fe3O4 Nanocomposites and Its Antibacterial Properties. *Materials* **2016,** *9* (7).
14. Nguyen-Tri, P.; Nguyen, T. A.; Carriere, P.; Ngo Xuan, C., Nanocomposite Coatings: Preparation, Characterization, Properties, and Applications. *International Journal of Corrosion* **2018,** *2018*, 1-19.
15. Pyun, J.; Jia, S.; Kowalewski, T.; Patterson, G. D.; Matyjaszewski, K., Synthesis and Characterization of Organic/Inorganic Hybrid Nanoparticles: Kinetics of Surface-Initiated Atom Transfer Radical Polymerization and Morphology of Hybrid Nanoparticle Ultrathin Films. *Macromolecules* **2003,** *36* (14), 5094-5104.
16. Li, X.; Ji, N.; Li, M.; Zhang, S.; Xiong, L.; Sun, Q., Morphology and Structural Properties of Novel Short Linear Glucan/Protein Hybrid Nanoparticles and Their Influence on the Rheological Properties of Starch Gel. *Journal of Agricultural and Food Chemistry* **2017,** *65* (36), 7955-7965.
17. Nguyen Tri, P.; Guinault, A.; Sollogoub, C., Élaboration et propriétés des composites polypropylène recyclé/fibres de bambou. *Matériaux & Techniques* **2012,** *100* (5), 413-423.
18. Azizi, S.; David, E.; Fréchette, M. F.; Nguyen-Tri, P.; Ouellet-Plamondon, C. M., Electrical and thermal conductivity of ethylene vinyl acetate composite with graphene and carbon black filler. *Polymer Testing* **2018,** *72*, 24-31.
19. Azizi, S.; David, E.; Fréchette, M. F.; Nguyen-Tri, P.; Ouellet-Plamondon, C. M., Electrical and thermal phenomena in low-density polyethylene/carbon black composites near the percolation threshold. *Journal of Applied Polymer Science* **2018**, 47043.
20. Boukehili, H.; Nguyen-Tri, P., Helium gas barrier and water absorption behavior of bamboo fiber reinforced recycled polypropylene. *Journal of Reinforced Plastics and Composites* **2012,** *31* (23), 1638-1651.
21. Nguyen Tri, P.; Gilbert, V., Non-isothermal Crystallization Kinetics of Short Bamboo Fiber-reinforced Recycled Polypropylene Composites. *Journal of Reinforced Plastics and Composites* **2010,** *29* (17), 2576-2591.
22. Nguyen Tri, P.; Sollogoub, C.; Guinault, A., Relationship between fiber chemical treatment and properties of recycled pp/bamboo fiber composites. *Journal of Reinforced Plastics and Composites* **2010,** *29* (21), 3244-3256.
23. Nguyen Tri, P.; Nguyen, T. A.; Nguyen, T. H.; Carriere, P., Antibacterial Behavior of Hybrid Nanoparticles. **2019**, 141-155.
24. Tri, P. N.; Rtimi, S.; Nguyen, T. A.; Vu, M. T., Physics, Electrochemistry, Photochemistry, and Photoelectrochemistry of Hybrid Nanoparticles. **2019**, 95-123.
25. Nguyen Tri, P.; Ouellet-Plamondon, C.; Rtimi, S.; Assadi, A. A.; Nguyen, T. A., Methods for Synthesis of Hybrid Nanoparticles. **2019**, 51-63.
26. Nguyen, T. V.; Nguyen Tri, P.; Nguyen, T. D.; El Aidani, R.; Trinh, V. T.; Decker, C., Accelerated degradation of water borne acrylic nanocomposites used in outdoor protective coatings. *Polymer Degradation and Stability* **2016,** *128*, 65-76.

27. Nguyen Tri, P.; Prud'homme, R. E., Crystallization and Segregation Behavior at the Submicrometer Scale of PCL/PEG Blends. *Macromolecules* **2018,** *51* (18), 7266-7273.
28. Nguyen, T. P., Nanoscale analysis of the photodegradation of Polyester fibers by AFM-IR *Journal of Photochemistry and Photobiology A: Chemistry* **2018,** *Accepted*.
29. Tri, P. N.; Prud'homme, R. E., Nanoscale Lamellar Assembly and Segregation Mechanism of Poly(3-hydroxybutyrate)/Poly(ethylene glycol) Blends. *Macromolecules* **2018,** *51* (1), 181-188.
30. Satyabrata, M. T., Anh Nguyen; Phuong, Nguyen-Tri;, *Noble Metal-Metal Oxide Hybrid Nanoparticles*. Elsevier: 2018; Vol. 1.
31. El Aidani, R.; Nguyen-Tri, P.; Malajati, Y.; Lara, J.; Vu-Khanh, T., Photochemical aging of an e-PTFE/NOMEX® membrane used in firefighter protective clothing. *Polymer Degradation and Stability* **2013,** *98* (7), 1300-1310.
32. Zeb, G.; Tri, P. N.; Palacin, S.; Le, X. T., Pulse potential deposition of thick polyvinylpyridine-like film on the surface of titanium nitride. *RSC Adv.* **2016,** *6* (84), 80825-80829.
33. Nguyen, T. V.; Le, X. H.; Dao, P. H.; Decker, C.; Nguyen-Tri, P., Stability of acrylic polyurethane coatings under accelerated aging tests and natural outdoor exposure: The critical role of the used photo-stabilizers. *Progress in Organic Coatings* **2018,** *124*, 137-146.
34. Cowcher, D. P.; Deckert-Gaudig, T.; Brewster, V. L.; Ashton, L.; Deckert, V.; Goodacre, R., Detection of Protein Glycosylation Using Tip-Enhanced Raman Scattering. *Analytical Chemistry* **2016,** *88* (4), 2105-2112.
35. Huang, S.; Pandey, R.; Barman, I.; Kong, J.; Dresselhaus, M., Raman Enhancement of Blood Constituent Proteins Using Graphene. *ACS Photonics* **2018,** *5* (8), 2978-2982.
36. Dazzi, A.; Prater, C. B., AFM-IR: Technology and Applications in Nanoscale Infrared Spectroscopy and Chemical Imaging. *Chemical Reviews* **2017,** *117* (7), 5146-5173.
37. Hartman, T.; Wondergem, C. S.; Kumar, N.; van den Berg, A.; Weckhuysen, B. M., Surface- and Tip-Enhanced Raman Spectroscopy in Catalysis. *The Journal of Physical Chemistry Letters* **2016,** *7* (8), 1570-1584.
38. Koutzarova, T.; Kolev, S.; Ghelev, C.; Paneva, D.; Nedkov, I., Microstructural study and size control of iron oxide nanoparticles produced by microemulsion technique. *physica status solidi (c)* **2006,** *3* (5), 1302-1307.
39. Rahman, O. u.; Mohapatra, S. C.; Ahmad, S., Fe3O4 inverse spinal super paramagnetic nanoparticles. *Materials Chemistry and Physics* **2012,** *132* (1), 196-202.
40. Kuriakose, S.; Choudhary, V.; Satpati, B.; Mohapatra, S., Enhanced photocatalytic activity of Ag-ZnO hybrid plasmonic nanostructures prepared by a facile wet chemical method. *Beilstein J Nanotechnol* **2014,** *5*, 639-50.
41. Mandal, S.; Wang, J.; Winans, R. E.; Jensen, L.; Sen, A., Quantum Size Effects in the Optical Properties of Ligand Stabilized Aluminum Nanoclusters. *The Journal of Physical Chemistry C* **2013,** *117* (13), 6741-6746.
42. Peng, S.; McMahon, J. M.; Schatz, G. C.; Gray, S. K.; Sun, Y., Reversing the size-dependence of surface plasmon resonances. *Proceedings of the National Academy of Sciences* **2010,** *107* (33), 14530-14534.
43. Xu, S.; Hartvickson, S.; Zhao, J. X., Engineering of SiO2−Au−SiO2 Sandwich Nanoaggregates Using a Building Block: Single, Double, and Triple Cores for Enhancement of Near Infrared Fluorescence. *Langmuir* **2008,** *24* (14), 7492-7499.
44. Siiman, O.; Bumm, L. A.; Callaghan, R.; Blatchford, C. G.; Kerker, M., Surface-enhanced Raman scattering by citrate on colloidal silver. *The Journal of Physical Chemistry* **1983,** *87* (6), 1014-1023.
45. Chudasama, B.; Vala, A. K.; Andhariya, N.; Upadhyay, R. V.; Mehta, R. V., Enhanced antibacterial activity of bifunctional Fe3O4-Ag core-shell nanostructures. *Nano Research* **2009,** *2* (12), 955-965.

46. Buszewski, B.; Railean-Plugaru, V.; Pomastowski, P.; Rafinska, K.; Szultka-Mlynska, M.; Golinska, P.; Wypij, M.; Laskowski, D.; Dahm, H., Antimicrobial activity of biosilver nanoparticles produced by a novel Streptacidiphilus durhamensis strain. *J Microbiol Immunol Infect* **2018,** *51* (1), 45-54.

47. Banach, M.; Tymczyna, L.; Chmielowiec-Korzeniowska, A.; Pulit-Prociak, J., Nanosilver Biocidal Properties and Their Application in Disinfection of Hatchers in Poultry Processing Plants. *Bioinorg Chem Appl* **2016,** *2016*, 5214783.

48. Bao, H.; Yu, X.; Xu, C.; Li, X.; Li, Z.; Wei, D.; Liu, Y., New toxicity mechanism of silver nanoparticles: promoting apoptosis and inhibiting proliferation. *PLoS One* **2015,** *10* (3), e0122535.

49. Wakshlak, R. B.; Pedahzur, R.; Avnir, D., Antibacterial activity of silver-killed bacteria: the "zombies" effect. *Sci Rep* **2015,** *5*, 9555.

50. Žagar, E.; Grdadolnik, J., An infrared spectroscopic study of H-bond network in hyperbranched polyester polyol. *Journal of Molecular Structure* **2003,** *658* (3), 143-152.

51. Lu, J. F.; Tsai, C. J., Hydrothermal phase transformation of hematite to magnetite. *Nanoscale Res Lett* **2014,** *9* (1), 230.

52. Bellot-Gurlet, L.; Neff, D.; Réguer, S.; Monnier, J.; Saheb, M.; Dillmann, P., Raman Studies of Corrosion Layers Formed on Archaeological Irons in Various Media. *Journal of Nano Research* **2009,** *8*, 147-156.

53. Schie, I. W.; Nolte, L.; Pedersen, T. L.; Smith, Z.; Wu, J.; Yahiatene, I.; Newman, J. W.; Huser, T., Direct comparison of fatty acid ratios in single cellular lipid droplets as determined by comparative Raman spectroscopy and gas chromatography. *Analyst* **2013,** *138* (21), 6662-70.